Pergamon

Geochimica et Cosmochimica Acta, Vol. 63, No. 3/4, pp. 337–350, 1999

0016-7037/−1801 $20.00 + .00

PII S0016-7037(99)00056-3

Chemical weathering in a tropical watershed, Luquillo Mountains, Puerto Rico III: Quartz dissolution rates

MARJORIE S. SCHULZ,[1,*] and ART F. WHITE[1]
[1]U.S. Geological Survey, Menlo Park, CA 94025 USA

(*Received May* 15, 1998; *accepted in revised form November* 4, 1998)

Abstract—The paucity of weathering rates for quartz in the natural environment stems both from the slow rate at which quartz dissolves and the difficulty in differentiating solute Si contributed by quartz from that derived from other silicate minerals. This study, a first effort in quantifying natural rates of quartz dissolution, takes advantage of extremely rapid tropical weathering, simple regolith mineralogy, and detailed information on hydrologic and chemical transport. Quartz abundances and grain sizes are relatively constant with depth in a thick saprolite. Limited quartz dissolution is indicated by solution rounding of primary angularity and by the formation of etch pits. A low correlation of surface area (0.14 and 0.42 $m^2\ g^{-1}$) with grain size indicates that internal microfractures and pitting are the principal contributors to total surface area.

Pore water silica concentration increases linearly with depth. On a molar basis, between one and three quarters of pore water silica is derived from quartz with the remainder contributed from biotite weathering. Average solute Si remains thermodynamically undersaturated with respect to recently revised estimates of quartz solubility ($<$180 μM) but exceeds estimated critical saturation concentrations controlling the initiation of etch pit formation ($>$17–81 μM). Etch pitting is more abundant on grains in the upper saprolite and is associated with pore waters lower in dissolved silica. Rate constants describing quartz dissolution increase with decreasing depth (from $10^{-14.5}$–$10^{-15.1}$ mol $m^{-2}\ s^{-1}$), which correlate with both greater thermodynamic undersaturation and increasing etch pit densities. Unlike for many aluminosilicates, the calculated natural weathering rates of quartz fall slightly below the rate constants previously reported for experimental studies ($10^{-12.4}$–$10^{-14.2}$ mol $m^{-2}\ s^{-1}$). This agreement reflects the structural simplicity of quartz, dilute solutes, and near-hydrologic saturation.

1. INTRODUCTION

Quartz comprises 20% by volume of the rocks exposed at the earth's crust and is ubiquitous in most silicate weathering environments (Nesbitt and Young, 1984). Experimental quartz dissolution studies at 25°C and at near neutral pH report dissolution rate constants of between $10^{-14.24}$ and $10^{-12.4}$ mol $m^{-2}\ s^{-1}$ (Rimstidt and Barnes, 1980; Brady and Walther, 1990; Bennett, 1991; Berger et al., 1994; Tester et al., 1994). These rates are one to several orders of magnitude slower than for other primary silicate minerals. Based on experimental rates, Lasaga (1984) estimated that a quartz grain, initially 1 mm in diameter, would persist in the natural weathering environment in excess of 30 Ma. Unlike for many other silicate phases, natural quartz weathering rates are generally not available to compare experimental rates against (White and Brantley, 1995). This omission stems both from the slow rate at which quartz dissolves and the difficulty in separating aqueous silica concentrations contributed by quartz dissolution from concurrent dissolution and precipitation reactions involving other silicate phases.

More qualitative estimates of quartz weathering, based on changes in mineral mass, morphology, and surface area, vary widely depending on the environmental conditions. Weathering studies of relatively young temperate regoliths report little evidence for quartz loss. These studies often consider quartz as an inert component relative to weathering rates of other silicate phases (Sverdrup, 1990; White et al., 1996). In contrast, extensive morphologic evidence, including development of grain rounding, etch pits, and fragmentation, have been documented for older, tropical soils, indicating extensive dissolution and concurrent silica mobility (Eswaran, 1979; Herbillon, 1980; Pye and Mazzullo, 1994; Malengreau and Sposito, 1997).

The present study quantifies natural rates of quartz weathering based on pore water chemistry, mineral surface areas, and fluid infiltration rates in a tropical saprolite within the Rio Icacos watershed in the Luquillo Mountains of Puerto Rico. This study takes advantage of extremely rapid weathering, a relatively simple regolith mineralogy, and detailed information on hydrologic and chemical transport. This work is the latest in a series of papers detailing rates of chemical weathering under tropical conditions within the Rio Icacos watershed (White et al., 1998; Murphy et al., 1998).

2. LOCATION AND METHODOLOGY

The study area is located on the Guaba Ridge (elevation 680 m), a *cuchillo* or knife edge feature separating two first-order streams in the Rio Icacos watershed (Fig. 1). Mean annual temperature is 22°C. Average rainfall is 4200 mm y^{-1} and is generally evenly distributed throughout the year. Consistently wet weather, warm temperatures, and steep topography provide ideal conditions for accelerated chemical weathering. A review of worldwide chemical discharge fluxes by White and Blum (1995) indicated that the Rio Icacos watershed has the highest weathering rates yet documented for granitoid rocks.

*Author to whom correspondence should be addressed (E-Mail: mschulz@usgs.gov.)

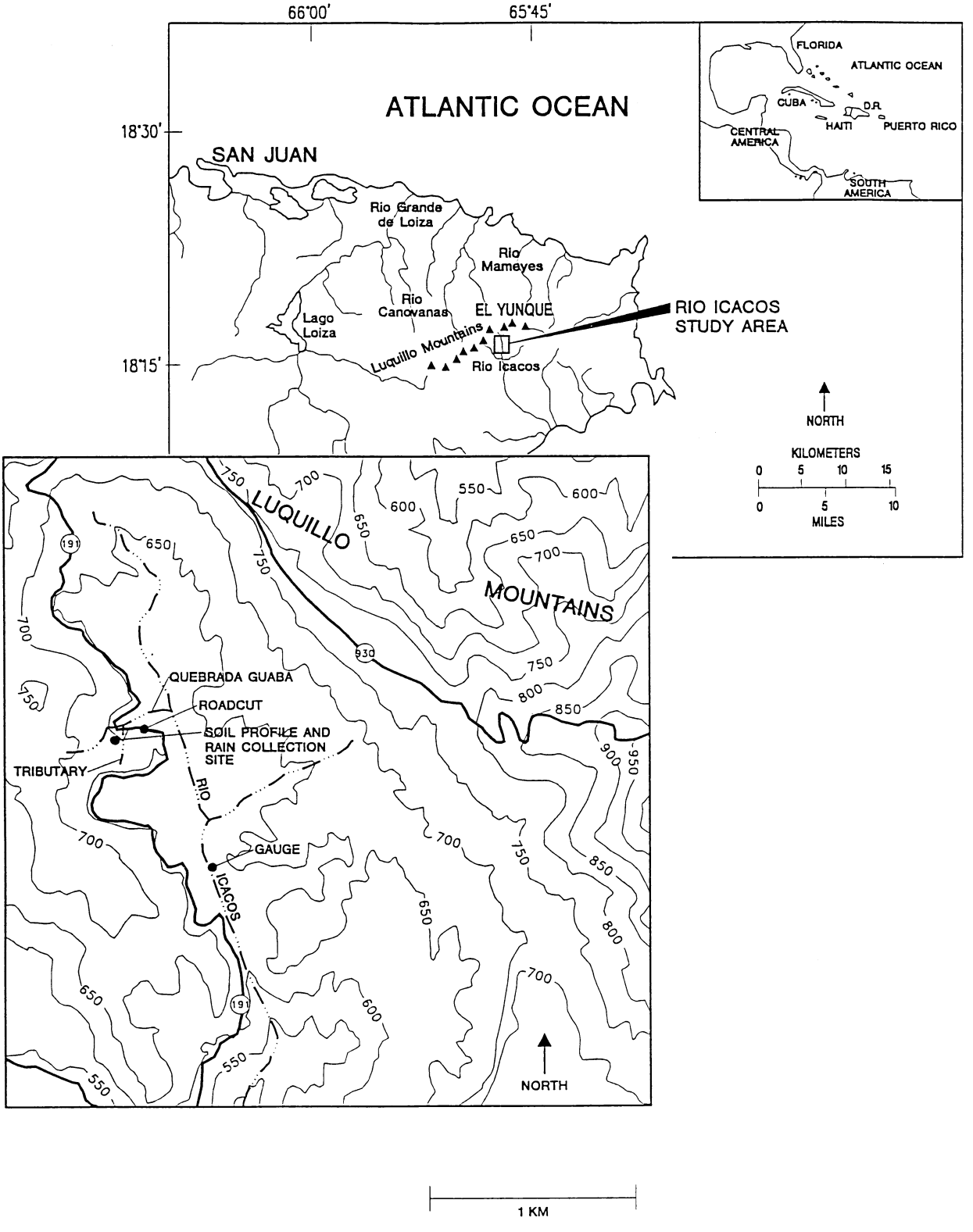

Fig. 1. Location maps showing the location of the Rio Icacos watershed and Guaba Ridge.

The Guaba Ridge is underlain by the Rio Blanco stock, a quartz diorite intrusion of early Tertiary age (Seiders, 1971). The Rio Blanco stock is medium to coarse grained and is dominated by quartz and plagioclase with lesser amounts of biotite, hornblende, and K-feldspar and accessory magnetite, sphene, apatite, and zircon. The shallowest portion of the overlying regolith on the Guaba Ridge consists of ultisols which have moderate to high permeability, moderate to low water retention capacity, medium fertility, and rapid runoff (Boccheciamp, 1977). The soil has a total thickness of 0.5–1.0 m and grades from a thin organic-rich A horizon (<0.10 m) to a clay-rich basal B horizon. The soil is bioturbated by earthworms and root throws. Below the soil is a 2–8 m thick oxidized saprolite, which retains the original bedrock texture. Variations in saprolite depth indicate that the bedrock does not have a smooth, regular surface but rather consists of core stones formed by weathering along fractures and joints. Measurement of ^{10}Be accumulation in quartz grains from an adjacent ridge top location indicates that the regolith surface has an age of approximately 200 Ka (Brown et al., 1995). Hillslope soil and saprolite are generally thinner than on the ridge tops, and hillslope weathering surfaces are much younger. Landslides on hillslopes are the principal mechanism of physical erosion in the Luquillo Mountains (Larsen and Torres-Sanchez, 1989; Simon et al., 1990).

Instruments, consisting of nested ceramic cup suction water samplers, analogue tensiometers, and gas samplers, were installed at three sites on the Guaba Ridge in 1992 (Fig. 1). The LG-1 site is on a relatively flat shoulder of the ridge top, LG-2 is situated on the hillslope, and LG-3 is situated on a relatively steep nose of the ridge top. Instrumentation at the 3 sites was installed to bedrock at respective depths of 8.5, 2.3, and 3.6 m. Bulk precipitation and throughfall collectors were installed, and surface waters were sampled in adjacent streams. Water samples were collected approximately bimonthly between October 1992 and March 1994. Samples of the regolith were taken from hand-augured holes. Bulk density and gravimetric samples were also obtained and cores taken for experimental hydraulic conductivity measurements.

Soil and saprolite splits were taken in the laboratory for surface area analyses. The splits were sieved and the >38-μm size fraction was ultrasonically cleaned and treated with citrate-bicarbonate-dithionite (CBD) to remove Fe-oxides (Mehra and Jackson, 1960). After completion of these procedures, the samples were composed predominately of quartz and altered biotite (White et al., 1998; Murphy et al., 1998). A Franz magnetic separator was used to diamagnetically separate pure quartz samples for surface area analyses. Single point N_2 Brunauer-Emmett-Teller (BET) surface area analyses were done with Micromeritics Flowsorb II 2300. Grains were examined with a scanning electron microscope (SEM), employing energy dispersive spectroscopy (EDS) and in thin section with a standard petrographic microscope. Grain size analyses of the Fe extracted samples (38–1000 μm diameter) were performed by laser scattering using a LS 100 Coulter Counter. Saturated hydraulic conductivities of the bulk soil were measured on cores using a falling head permeameter (Klute and Dirksen, 1986) and unsaturated conductivities were determined by steady state centrifugation (Nimmo et al., 1992).

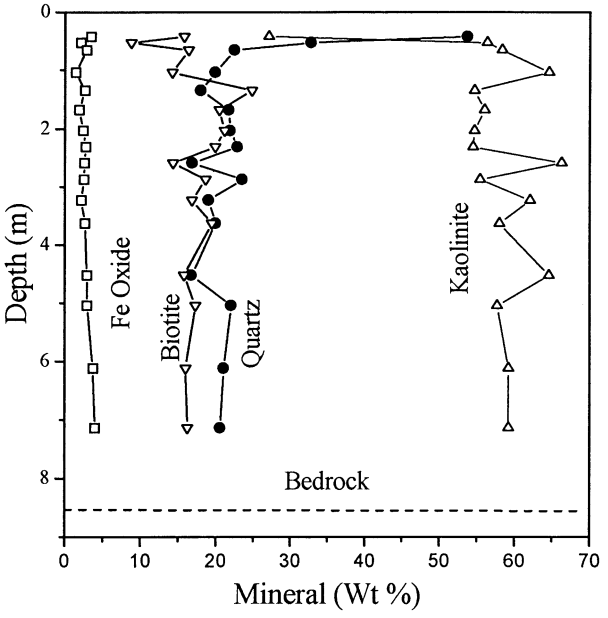

Fig. 2. Distribution of minerals and oxides (weight %) with depth within the Guaba Ridge weathering profile LG-1.

3. RESULTS

The following results detail the physical and chemical characteristics of quartz weathering and describe the associated hydrochemistry at the Guaba Ridge site. Except as noted, data pertain to the LG-1 site, which contains the deepest and longest record of chemical weathering.

3.1. Quartz Distribution

Quartz is present in approximately constant proportions (16–23 wt%) in the LG-1 saprolite (1.2–9.2 m) relative to altered biotite, kaolinite, and iron oxides (Fig. 2). In contrast, quartz comprises up to 53 wt% of the upper A soil horizon. This increase at shallow depth coincides with a corresponding decrease in kaolinite. K-feldspar and plagioclase persist in very limited amounts throughout the soil and saprolite (<1%) and exhibit extensive dissolution features (White et al., 1998).

Quartz grain size distributions in the Fe-extracted silt/sand fraction (38–1000 μm diameter) are essentially constant as a function of depth in the saprolite as shown in detail by the plot of weight fraction of given phi intervals from 0.66–1.78 m depth (Fig. 3). The mean average grain size is 450 μm. Such similarity indicates that the quartz size distribution in the original quartz diorite was homogeneous. Grain sizes have not been selectively reduced in the saprolite by subsequent dissolution, and fragmentation as has been observed in some tropical soils (Eswaran, 1979).

The only significant variation in quartz size distribution occurs in a coarse-grained (average size, 1800 μm) quartz-rich layer at a depth of 0.40 m. Thin section analyses indicate that this layer consists of large individual quartz grains. Similar coarse-grained quartz has been observed in other tropical soils and has been attributed to selective removal of finer grained

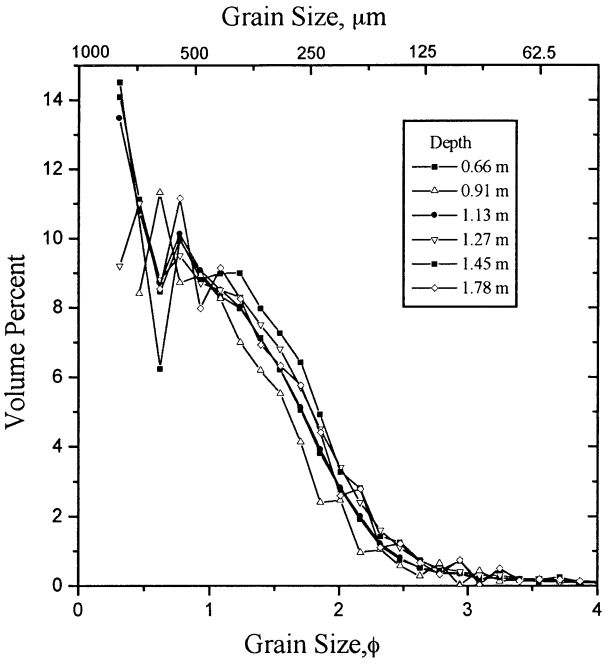

Fig. 3. Grain size distribution within the saprolite at depths from 0.66 to 1.78 m. Size fractions >1000 and <38 μm were removed prior to this analysis.

material by a combination of sheet wash and bioturbation. (Nooren et al., 1995; Thomas, 1994).

3.2. Quartz Morphology

Quartz surface morphology is commonly used to estimate the age and the extent of chemical weathering (Douglas and Platt, 1977; Darmody, 1985; Marcelino and Stoops, 1996). Quartz grain morphologies in the Rio Icacos saprolite developed in situ, as a result of initial crystallization in the pluton and subsequent weathering processes. Quartz grains, characterized by both thin sections and SEM grain mounts, are generally angular to very angular. Quartz is among the last minerals to crystallize from a magma, and grain morphology is controlled by previously established mineral fabrics. Quartz becomes intergrown with other minerals in complex three-dimensional interdigitated morphologies. Many quartz grains contain holes and embayments (re-entrants). Although rounded quartz embayments in other studies have been ascribed to dissolution (Crook, 1968; Cleary and Conolly, 1972), embayments and holes in the Guaba Ridge quartz are due primarily to the preferential dissolution of embedded and included grains such as feldspar (Fig. 4A and B).

Quartz grains at all depths in the Guaba Ridge regolith exhibit hairline microfractures (Fig. 4A). These fractures tend to be subparallel and subplanar in nature; they are not cleavages and are not related to quartz crystallography. When grains break they tend to split along these microfractures, creating surfaces that are relatively flat and grains that are tabular in shape. Microfractures are ubiquitous in plutonic quartz (Blatt, 1967; Moss and Green, 1975; Mazzullo and Magenheimer, 1987; Asumadu et al., 1987; Pye and Mazzullo, 1994; Pope, 1995) and are commonly attributed to normal stresses between the time of crystallization and emergence. Part of this fracturing may result from local tectonic deformation and part from the inherent nature of igneous quartz crystallization. Quartz crystallizes as β (or high) quartz and inverts to α (or low) quartz upon cooling below 573°C. This transformation is accompanied by a volume decrease of 0.86% (Raeside, 1959), which contributes to stressing and microfracturing of interdigitated quartz grains. Microfractures have led to significant fragmentation of quartz grains in other weathering environments (Pye and Mazzullo, 1994; Pye and Sperling, 1983). Although somewhat friable, quartz grains in the present study have not undergone significant fragmentation based on a lack of grain size reduction (Fig. 3).

Microfractures subsequently provide pathways for fluid transport into the quartz grain interiors. Evidence of dissolution along microfractures in quartz grains has been reported in several studies (Asumadu et al., 1988; Pye and Mazzullo, 1994; Crook, 1968; Pope, 1995). At the shallowest depths in the Guaba Ridge soil, fractures in quartz grains are commonly filled with Fe-oxides that were not removed by multiple CDB Fe-extractions (Fig. 4A). Quartz fractures filled with kaolinite, goethite, hematite, and gibbsite have been observed in other tropical soils and have been defined as *runi-quartz* based on their red coloration (Eswaran, 1979). Chemical corrosion of fracture walls associated with these secondary phases is also sometimes observed (Pope, 1995).

SEM examination of the Guaba Ridge quartz grains indicates significant variations in surface morphology and etch pit size and density (Fig. 4C–F). Etch pits range from typical triangular pits (Fig. 4D) to pits that have elongated and coalesced (Fig. 4E and F). At any one depth there is a diversity of surfaces present, some grains are highly etched, and others appear fairly pristine. Such differences in etch pit density can be attributed to differences in crystallographic orientation (Hicks, 1985; Gratz et al., 1991) and/or to variations in microweathering environments.

3.3. Surface Area of Quartz

BET surface area measurements were made on the cleaned quartz size fractions (150–1000 μm). Data (Table 1) are plotted as a function of grain size and depth in Fig. 5. The uppermost soil sample (0.56 m) has relatively high surface areas (0.15–0.42 $m^2\ g^{-1}$), whereas underlying upper saprolite at 2.3 m has a lower range in surface areas (0.14–0.20 m^{-2} g). Deeper in the saprolite, surface areas exhibit a linear increase with increasing depth and reach a maximum range in surface area at the saprolite/granite interface (0.31–0.40 $m^2\ g^{-1}$ at 7.14 m). These ranges in surface areas, which vary by a factor of about 3, are comparable to those measured on quartz from granitic alluvium (0.01–0.23 $m^2\ g^{-1}$) by White et al. (1996). Weathered quartz surface areas are significantly lower than commonly measured for weathered aluminosilicate minerals (Brantley et al., 1998).

3.4. Pore Water Silica Concentrations

White et al. (1998) and Murphy et al. (1998) discuss in detail the chemical compositions of precipitation and pore waters collected from the Guaba Ridge. The average pore waters are

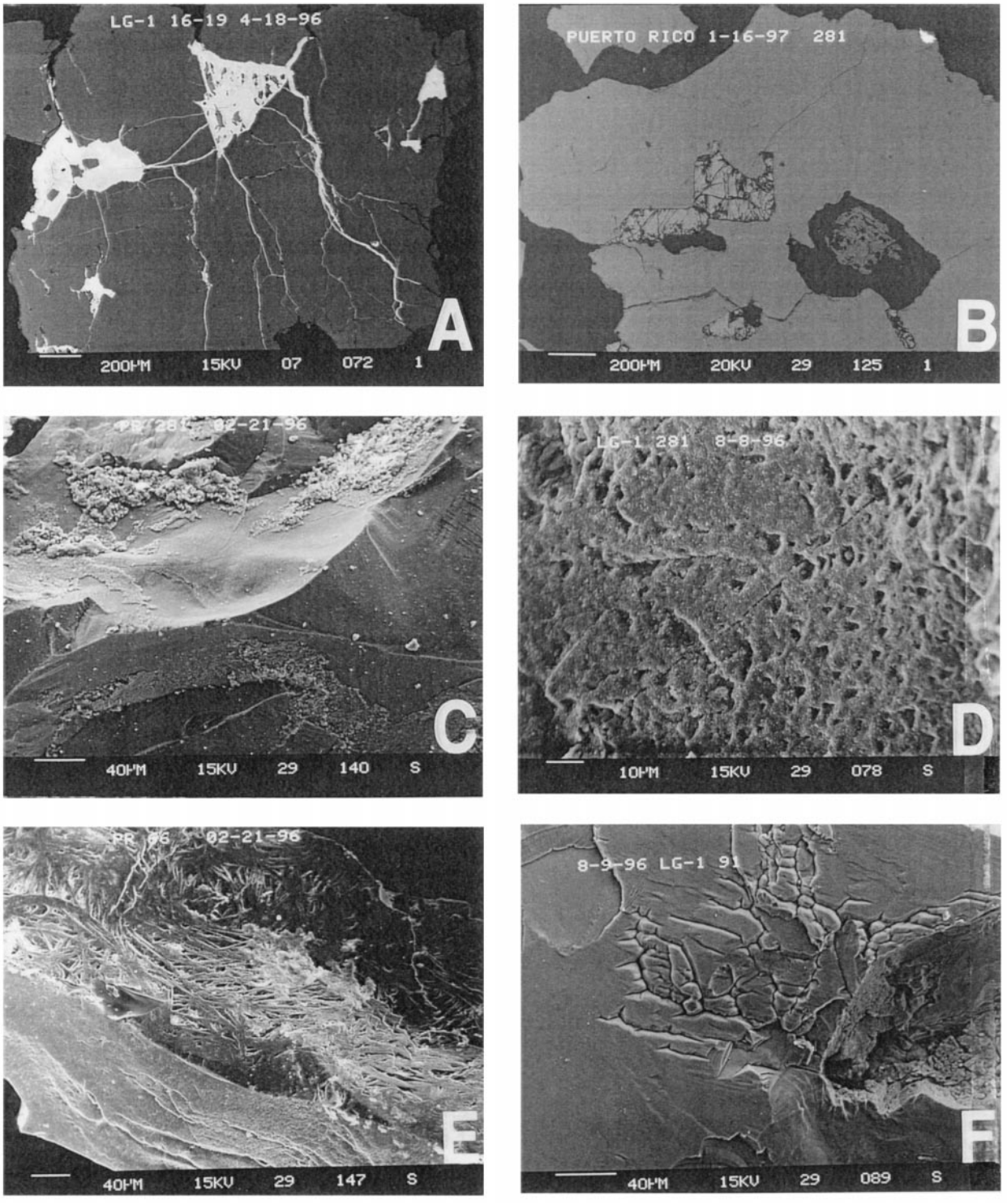

Fig. 4. SEM photomicrographs of quartz grains from the LG-1 weathering profile. All grains have been through CBD Fe-extractions and sonicated to remove fines. (A) Backscattered image of a thin sectioned quartz grain from the soil (0.45 m). The bright areas are iron rich materials. (B) Backscattered image of thin sectioned quartz grain from the bottom of the weathering profile (7.14 m) showing a highly weathered inclusion of K-feldspar, microfractures, and a hole with a clay filling, that are likely secondary products from a fully weathered feldspar. (C) Quartz grain from 7.14 m depth showing a smooth surface with a patchy coating of a clay-like material not removed by sonication. EDS analysis shows Al $\cong$ Si. (D) Surface of a quartz grain from 7.14 m depth illustrating a typical rough surface with triangular etch pits. (E) Surface of a quartz grain from 1.68 m depth showing a surface completely covered by coalesced etch pits next to a relatively smooth surface. (F) Surface of a quartz grain from 2.31 m depth showing coalesced etch pits and a hole left by a weathered-out inclusion.

Table 1. Surface area data (BET) of quartz grains form several depths ($m^2\ g^{-1}$).

	Grain size interval (μm)					
Depth (m)	150–250	250–425	425–600	600–1000	1000–1180	1180–2000
0.56	0.42	0.15	0.16	0.22	0.27	0.32
2.31	0.20	0.14	0.19	0.16	0.21	0.20
3.63	0.24	0.22	0.20	0.17	0.25	0.26
4.52	0.25	0.25	0.25	0.28	0.27	0.31
714	0.39	0.33	0.31	0.37	0.40	0.39

dilute and mildly acidic (Table 2). Silica concentrations ranged between 16 and 383 μM, with a mean average of 103 μM. Dissolved silica measured in open and throughfall precipitation is negligible (<10 μM). Pore water silica concentrations are plotted as functions of depth at the three Guaba Ridge sites in Fig. 6.

The greatest temporal variability in solute concentration occurs in the upper soil (Fig. 6) due to evapotranspiration and recycling of silica through the vegetative cover and shallow root system (Lucas et al., 1993; Alexandre et al., 1997). Pore water Si showed minor temporal variations below the rooting depth (>1 m). Silica increased linearly with depth in the LG1 saprolite (Fig. 6). A linear regression fit to the data below 1.2 m (Fig. 6, diagonal line) predicts an average silica increase of 28 μM m^{-1}($r^2 = 0.74$). Silica increased with depth in pore waters at the LG-2 and LG-3 sites (Fig. 6). However, a linear trend is less apparent due to a thinner saprolite sequence. Higher and more variable Si concentrations also occurred in the deepest samplers at the LG-2 and LG-3 sites due to water movement down slope along the bedrock/saprolite interface during periods of high precipitation and runoff.

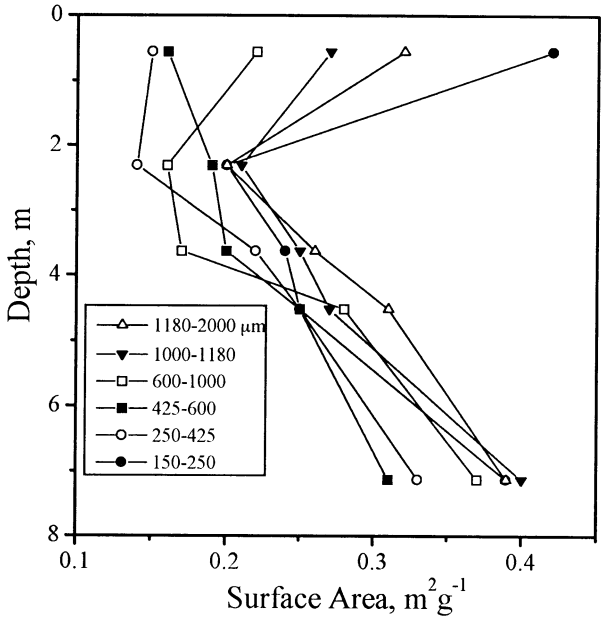

Fig. 5. BET surface areas of various quartz grain size fractions with depth.

3.5. Infiltration Rates

White et al. (1998) and Stonestrom et al. (1998) discuss in detail porosity, permeability, and rates of pore water movement in the Guaba Ridge regolith. Porosities determined from bulk density and specific gravity are high throughout the regolith, decreasing from 75% in the upper bioturbated soil to a relatively constant porosity of 45% throughout the underlying saprolite. Undersaturated moisture conditions persist through the regolith (66–94% of saturation), except for perched groundwater in the immediate vicinity of the saprolite/bedrock interface. Pressure heads, as measured by field tensiometers, decrease linearly in the soil and upper saprolite (from -0.3 m H_2O to -1.9 m H_2O), indicating both increasing capillary tension and graviometric potential with depth.

Both saturated and unsaturated hydraulic conductivities were experimentally measured on cores of the Guaba Ridge saprolite (White et al., 1998; Stonestrom et al., 1998). Extrapolating average field saturation onto the experimental conductivity curve gives an average flux density of 6.14×10^{-9} m s^{-1}. This translates into an infiltration rate of approximately 0.6 m yr^{-1} and a fluid residence time of 12 years for pore water in the LG-1 profile. This is a factor of 2 slower than infiltration rates determined from Li-Br tracer tests (Turner et al., 1996) and watershed hydrologic balances (White et al., 1998).

4. DISCUSSION

The preceding results describing the distribution and morphology of quartz grains, solute silica concentrations, and fluid infiltration rates provide a framework for evaluating the weathering mechanisms and rates of quartz dissolution in the Guaba Ridge regolith. The following discussion explores the thermodynamic and kinetic constraints controlling observed natural quartz weathering and compares these results to those based on previous theoretical and experimental studies.

4.1. Quartz Thermodynamic Saturation and Etch Pit Formation

The solubility of quartz near 25°C has been extensively investigated but remains ambiguous in terms of delineating small differences in the approach to quartz saturation in natural systems. The most commonly cited quartz solubility values at 25°C are between 100–110 μM (Morey and Hesselgesser, 1951; Robie et al., 1979; Fournier and Potter, 1982). Rimstidt (1984) predicted a higher quartz solubility of 180 μM based on extrapolation of solubility experiments conducted between 50° and 90°C. Long-term solubility experiments at 25°C recently

Table 2. Average chemical composition of pore waters from the LG1 site (μM).

Depth (m)	1.22	1.52	1.83	2.44	3.66	5.49	7.47	8.53
pH	4.03	4.64	4.91	4.97	3.94	5.47	5.52	5.12
Alk	—	0.01	0.01	0.03	—	0.01	0.03	0.07
Na	70.3	91.6	102.5	116.9	120.6	167.7	160.4	155.7
K	5.19	4.97	5.60	17.76	6.60	26.29	27.36	38.41
Ca	7.32	9.68	8.66	9.63	6.65	19.35	4.54	27.47
Mg	11.2	12.8	32.5	25.0	20.0	49.4	43.8	59.0
Li	–	0.70	1.93	2.50	—	8.33	8.26	5.17
Mn	0.22	0.54	1.08	1.25	0.65	2.74	4.15	3.52
Fe	—	0.14	0.36	0.13	0.23	2.78	2.48	0.35
Al	9.06	3.07	3.47	1.07	7.26	4.31	2.35	19.84
SiO_2	60.7	63.3	68.0	117.0	87.3	166.0	169.6	213.5
Sr	0.03	0.08	0.10	0.06	0.03	0.14	0.06	0.13
Cl	128.1	126.1	149.6	143.3	168.9	255.9	198.0	171.1
NO_3	—	2.0	3.5	2.8	1.4	7.0	7.8	18.9
SO_4	12.4	10.7	10.3	8.6	10.4	5.3	7.0	7.6

reported by Rimstidt (1997) have confirmed the higher solubility. The following discussion shows how our data supports the higher quartz solubility.

Approximately 40% of the 400 silica pore water analyses from the Guaba Ridge exceed the 100 μM estimate for quartz thermodynamic saturation while less than 10% of the pore water silica concentrations exceed the revised 180 μM estimate for quartz saturation (Fig. 6, vertical lines). Although saturation is expected to limit quartz dissolution, it does not necessarily limit aqueous silica concentrations in pore waters. Pore waters that exceed quartz saturation (>180 μM) at shallow depth are concentrated by the effects of evapotranspiration. High silica concentrations deep in the saprolite, such as at the LG-1 site, reflect additional silica contributed from other phases, principally biotite. Murphy et al. (1998) discusses in detail the rate of biotite dissolution at the Guaba Ridge site. There is no evidence that quartz or other silica polymorphs precipitate as overgrowths or as secondary phases.

Etch pit formation and solution rounding provide indirect evidence that quartz is thermodynamically undersaturated and is dissolving in the regolith. Based on Monte Carlo simulations, Lasaga and Blum (1986) and Blum et al. (1990) suggested that etch pit formation at sites of dislocations in quartz could be an indicator of the degree of thermodynamic undersaturation of a solution. Brantley et al. (1986) linked the formation of etch pits on quartz grains to a critical silica concentration C_{crit} defined as

$$C_{crit} = C_0 e \left(\frac{-2\pi^2\gamma^2 V}{RTKb^2} \right) \quad (1)$$

where C_o is the equilibrium concentration (assumed here to be 180 μM, Rimstidt, 1997), γ is the interfacial energy of the surface (or surface free energy) (mJ m^{-2}), V is the molar volume (m^3), R is the gas constant (8.31 J $°K^{-1}$ mol^{-1}), T is temperature in °K, K is an energy factor (J m^{-3}) based on the type of dislocation, and *b* is the Burgers vector of the dislocation (m). Above the critical concentration (C_{crit}), the energy increase associated with increased surface area created by etch pit formation exceeds the energy loss associated with removal of the defect, and etch pit formation will not occur. Below C_{crit} the surface energy is less and pitting will occur.

The Burgers vectors, *b*, (Eqn. 1) are reasonably well constrained for quartz, ranging from 4.913 for the <0001> slip plane and 7.304 for the <0110> plane (Heinisch et al., 1975). Values of K are dependent on the type of dislocation and are expected to vary only moderately from 0.397 to 0.533 J m^{-3} (Heinisch et al., 1975). Our calculations (Eqn. 1) use K values for the corresponding Burgers vectors of 0.447 and 0.446 J m^{-3}. Using both estimates of the quartz interfacial energy (416 mJ/m^2, Iler, 1979; 350 mJ/m^2, Parks, 1984) and *b* and K values for two slip systems of quartz results in four estimates for critical pitting concentrations (C_{crit}) that range between 17 and 81 μM (Fig. 7).

Dissolution of the quartz surface should occur at any silica concentration below thermodynamic saturation C_{sat} (Fig. 7, vertical line) but should not result in pitting at concentrations between C_{crit} and C_{sat}. The mean concentration and standard deviation for silica concentrations in the Guaba Ridge pore waters are also plotted in Fig. 7. The average silica concentration falls above the C_{crit} values, indicating that etch pits should not form under most pore water conditions in the regolith. This is in agreement with the observation that etch pitting is not observed on the majority of quartz surfaces. Etch pitting in quartz is strongly orientation dependant. Highly etched surfaces were observed adjacent to smooth unetched surfaces on the Guaba Ridge quartz grains.

A smaller subset of silica concentrations are more dilute than C_{crit} for the <0001> slip plane indicating limited pore water environments in which pitting can occur. The optimum environment for surface pitting is in the upper saprolite, which lies below the zone of silica concentration by evapotranspiration and biologic cycling and above the deeper saprolite in which silica concentrations increase due to cumulative quartz and biotite reaction (Fig. 6). This is in agreement with observed increased etch pitting on quartz at shallow depths in tropical regoliths as described by Brantley et al. (1986). The above conclusions must be tempered within the context of uncertainties involved in the calculations and the fact that past pore water chemistry may have varied from present conditions.

4.2. Effects of Weathering on Quartz Surface Areas

Calculation of natural weathering rates is strongly dependent on estimated surface areas. The measured BET surface areas of Guaba Ridge quartz grains do not increase consistently with

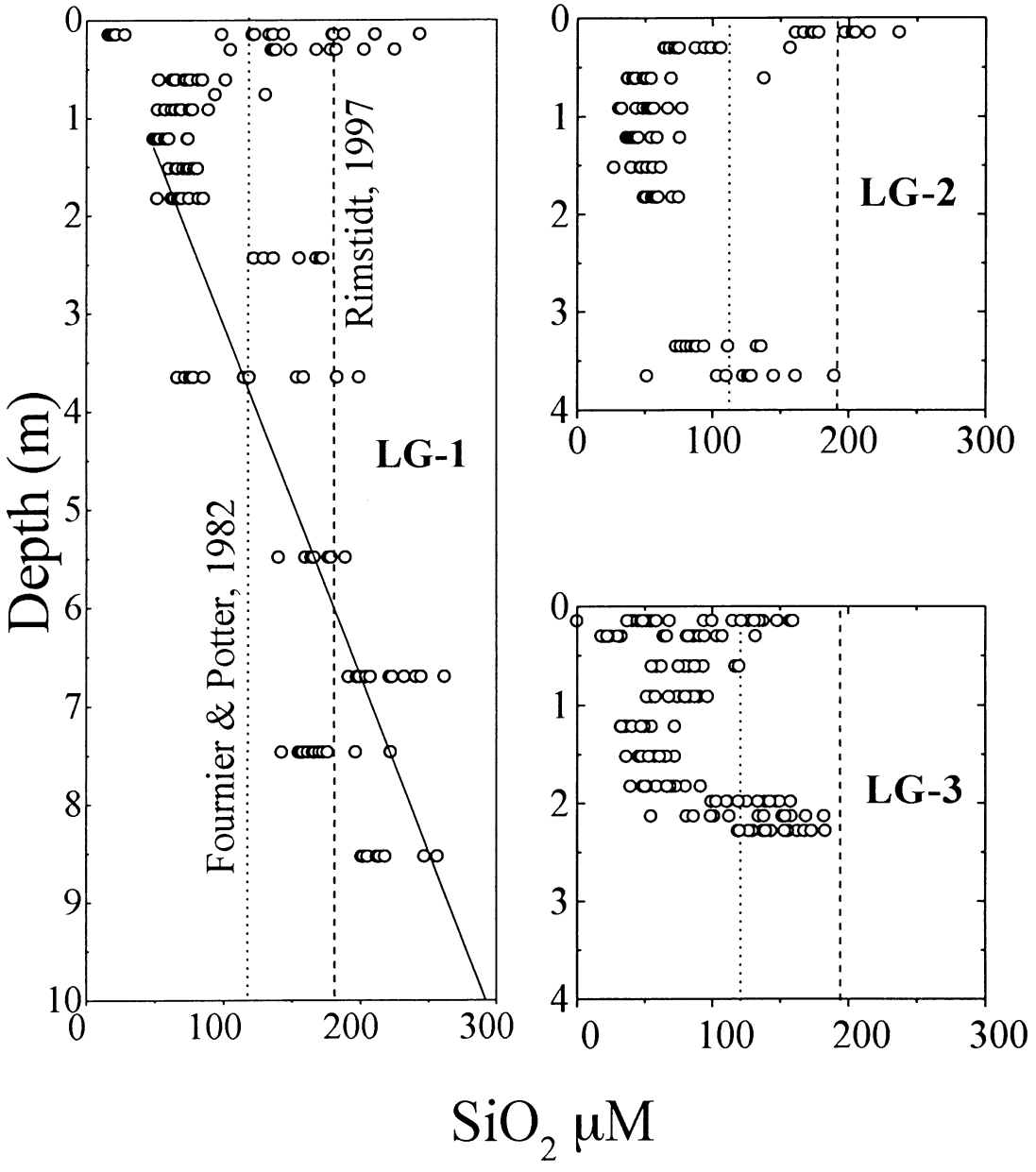

Fig. 6. Vertical distributions of silica in pore waters at 3 sites on the Guaba Ridge. Dotted line is quartz equilibrium concentration of Fournier and Potter (1982). Dashed line is quartz equilibrium concentration of Rimstidt (1997). Diagonal line is linear regression fit to the LG-1 data at depths >1.2 m.

decreasing profile depth and by inference longer weathering times. Surface areas are high in the soil, decrease to lower values in the upper saprolite, and increase again to the bottom of the profile (Fig. 5).

The total surface area of quartz grains is the sum of external area based on surface grain morphology and internal area based on grain porosity. The measured specific BET surface area S_t of mineral grains ($m^2\ g^{-1}$) can be defined in terms of the expression (White et al., 1996)

$$S_t = \frac{6}{\rho D}\lambda + S_i \qquad (2)$$

The first term on the right side of Eqn. 2 is the external surface area of a spherical mineral grain where D is the particle diameter (cm), ρ is density (2.65g cm^{-3}), and λ is the surface roughness associated with surface morphology, primarily angularity and secondary etch pitting. The internal surface area (S_i, Eqn. 2) is the total area associated with grain porosity.

Several features contribute to the external surface area and roughness of the quartz grains; strong primary angularity, etch pit formation, and any adhering secondary weathering products not removed in the cleaning process (Fig. 4C). Angularity is formed as a result of crystallization of quartz grains and subsequent weathering from the quartz diorite matrix. As substan-

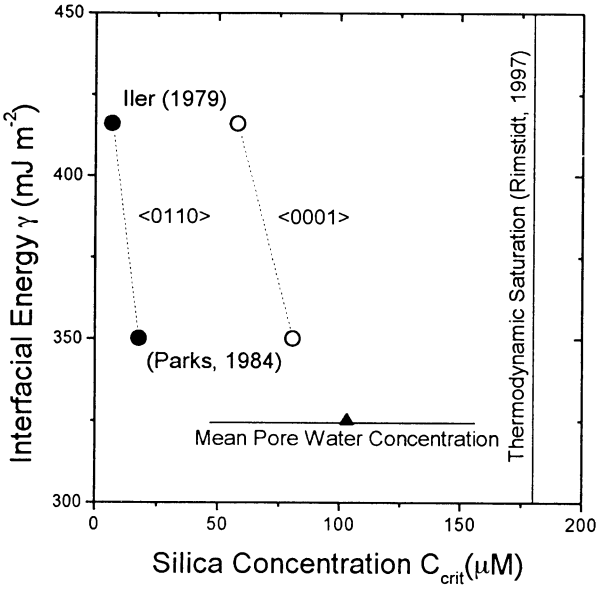

Fig. 7. Relationship between interfacial energies and solute silica concentrations. Open data points are calculated for the 4.913 burgers vector (<0001> slip plane) and closed points are for the 7.304 Burgers vector (<0110> slip plane>) (Heinisch et al., 1975). The upper and lower points are calculated with different interfacial energy values of Iler (1979) and Parks (1984). The triangular data point is the mean average pore water silica concentration with bar indicating standard deviation of pore water silica concentrations.

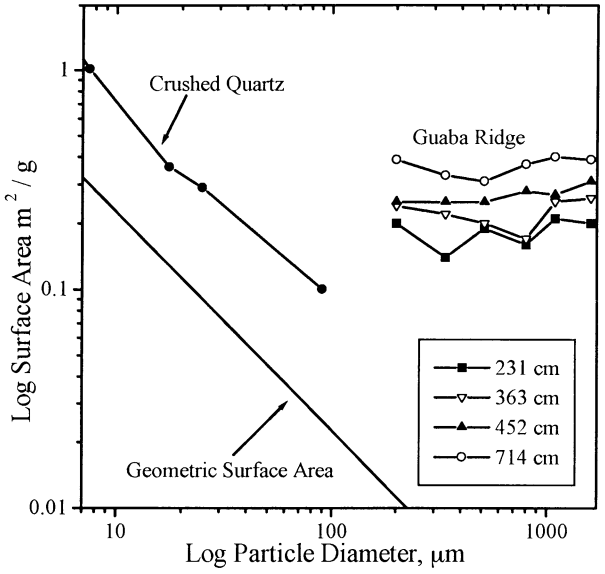

Fig. 8. Log of surface area as a function of log particle size for geometric surface areas of smooth spheres, BET surface areas of freshly crushed quartz (Leamnson et al., 1969), and BET surface areas of weathered quartz from different depths in Guaba Ridge.

tiated by SEM observations, rougher, more angular quartz grains occur in the deeper, younger portions of the saprolite closer to the bedrock interface. In the shallow saprolite and soil, quartz grains are smoother due to solution rounding as described for quartz weathering in other regoliths (Crook, 1968). Conversely, the density and size of etch pits associated with selective weathering of dislocations on the quartz surface increase with decreasing depth and increasing age in the saprolite, which is consistent with other etch pit studies in tropical saprolites (Brantley et al., 1986).

Whether external surface areas increase or decrease with weathering depends on the minimization in surface free energy associated with removal of dislocations by etch pitting (surface area increases) versus the loss of primary angularity by solution rounding (surface area decreases). Quantitative estimates of surface energy change associated with etch pit formation are discussed by Blum et al. (1990) and energy change during smooth surface dissolution is discussed by Gratz and Bird (1993). For most aluminosilicates with relatively high defect densities (undeformed K-feldspars $\approx 10^7$ cm^{-2}; Willaime et al., 1979), development of extensive etch pitting under most weathering conditions results in increased surface area (White and Brantley, 1995 and references therein). For quartz, which is closer to thermodynamic saturation and generally contains fewer dislocations ($<10^5$ cm^{-2}; Blum et al., 1990), the etch pit density is much lower. This may have the effect of increasing the importance of solution rounding for quartz, thus decreasing the external surface area contribution to Eqn. 2 with time.

The external surface/volume ratio is dependent on grain size (D in Eqn. 2). Therefore the total surface areas S_t of smaller particles are more sensitive to the external surface area ($S_t \approx 6\lambda/\rho D$) than are larger particles ($S_t \approx S_i$). A log-log plot of S_t versus D for mineral grains dominated by external surface area results in a slope which approaches -1 (Fig. 8) if the surface roughness is relatively constant with grain size. The similarity of this slope with that of the geometric surface is approximated by the crushed quartz surface area data of Leamnson et al. (1969) (Fig. 8) and for a large number of other relatively unweathered silicate phases (White and Peterson, 1990; Parks, 1990).

Eqn. 2 predicts that the total surface area of larger quartz particles will depend more than smaller grains on internal surface area produced by microfractures and holes. Some of these features retain residual minerals such as feldspars as evident in scanning electron micrographs (Fig. 4B). If this porosity is independent of particle diameter (i.e., these internal features are evenly distributed throughout the quartz grains), measured surface areas will become invariant with respect to grain size and a log-log plot of S_t versus D will approach a horizontal line. Based on linear regressions, the slopes defining S_t as a function of D for the Guaba Ridge quartz (Fig. 8) approach zero (i.e., 0.03 to 0.09), indicating that the surface areas are essentially independent of particle size. The BET surface areas (S_t) are therefore more dependent on the internal features within the quartz grains than on the more obvious external surface morphologies.

The relatively high BET surface areas of the quartz grains in the shallow soil (Fig. 5) correspond to the zone in which the internal microfractures are extensively infilled by secondary iron oxides which cannot be removed by conventional cleaning techniques (Fig. 4A). This infilling increases the total measured surface area due to the intrinsically larger specific surface areas of the iron oxide phase (goethite = 30–70 m^2 g^{-1}, Buffle, 1988). Iron mobility is increased in the shallow soil due to

Table 3. Masses of minerals reacted to produce average pore water compositions (mmol reacted per kg H_2O).*[1]

Constraints Depth (m)	Si, Al, Fe, Cl, K					Si, Al, Fe, Cl, Mg				
	Qtz	Biotite	Kaolinite	Goethite	Plag	Qtz	Biotite	Kaolinite	Goethite	Plag
1.52	8.7	−0.3	−0.3	5.3	0	8.8	−10.5	0.0	5.3	10.3
1.83	11.2	1.2	−3.9	−0.6	0	−19.9	25.2	−26.7	−12.6	0
2.44	38.7	19.7	−22.7	−9.9	0	50.1	10.9	−14.4	−5.5	0
3.66	34.7	5.9	−7.1	−2.9	0	18.9	18.0	−18.6	−9.02	0
5.49	69.7	32.0	−32.9	−13.0	0	41.4	53.8	−53.6	−23.9	0
7.47	72.7	33.5	−35.4	−15.8	0	58.0	44.8	−46.1	−21.4	0
8.53	80.7	52.0	−45.9	−26.0	0	55.2	71.6	−64.5	−35.8	0

* Positive number indicates dissolution, negative indicates precipitation.

[1] Mineral stoichiometries; Qtz = SiO_2, Goethite = FeOOH.

Kaolinite = $(K_{0.01}Fe_{0.07}Mg_{0.04})(Si_{2.21}Al_{1.69})O_5(OH)_4$, (Murphy et al., 1998), Biotite = $K_{0.65}(Al_{1.10}(Ti_{0.15}Fe^{2+}_{0.35}Fe^{3+}_{0.15}Mg_{0.55})(Si_{3.2}Al_{0.8})O_{10}(OH)_2$, Plagioclase = $Na_{0.60}Ca_{0.40}Al_{1.36}Si_{2.63}O_8$.

lower pH and higher organic contents in pore waters. *Runi* quartz is not observed in the underlying upper saprolite horizon where quartz grains have significantly lower total surface areas. The increase in surface area of the quartz grains with depth in the saprolite is counter to the observed decrease in surface etch pitting. The surface area increase is attributable to both increasing primary angularity and partially altered included feldspars at depth.

4.3. Mass Balance Within the Saprolite

Average pore water concentrations at various depths in the saprolite (Table 2) are modeled by reaction of quartz and other minerals using NETPATH (Plummer et al., 1991) (see White et al., 1998 for a more detailed discussion of this approach). Mineral stoichiometries specific to the Guaba Ridge regolith are used in the calculations (Table 3). Mineral mass changes were determined based on differences in average solute concentrations at the top of the saprolite (1.2 m) and concentrations at specific horizons deeper in the saprolite (1.5–8.5 m; Table 2). This approach was utilized rather than calculating mass balances between successive horizons because not all solute species increased consistently at each depth interval.

Reactions involving primary and secondary minerals in the soil and saprolite horizons are described by two sets of reaction constraints, K-Fe-Si-Al and Mg-Fe-Si-Al. These constraints contain 4 of the 5 elements that comprise the dominant mineral phases in the regolith (i.e. quartz, biotite, kaolinite, and goethite) (Fig. 2). Incorporation of additional constraints into a single calculation was not possible because solutions became overdetermined. This approach had an inherent advantage in that two sets of independent results could be compared to assess reproducibility in the calculations.

The potential reaction of kaolinite to gibbsite commonly observed in more intensely weathered tropical laterites (Nahon, 1991) was not considered in the calculations. The only evidence for kaolinite loss in the Guaba Ridge regolith occurs in the upper soil zone (Fig. 2) and is associated with low pH and elevated dissolved Al and DOC (White et al., 1998). Paragenesis of kaolinite is twofold in the underlying saprolite (Murphy et al., 1998; White et al., 1998). Fine-grained plasmogenic kaolinite (<2 μm), formed primarily from the dissolution of plagioclase at the bedrock/saprolite interface, remains constant in the saprolite, indicating minimal reaction. A second type of kaolinite, which pseudomorphically replaces biotite plates, increases upward in the saprolite (Murphy et al., 1998). Active formation of this form of kaolinite is consistent with demonstrated thermodynamic supersaturation in the saprolite pore waters (White et al., 1998). Elevated pore water silica due to quartz dissolution has been proposed to retard the weathering of kaolinite in other tropical soils (Herbillon, 1980; Malengreau and Sposito, 1997).

NETPATH results tabulated in Table 3 indicate that throughout most of the saprolite profile (2.4–8.5 m), changes in pore water Si, Al, Fe, K, and Mg can be described exclusively by dissolution of quartz and biotite (positive values, μmol per kg^{-1} H_2O) and precipitation of kaolinite and goethite (negative values). Primary plagioclase, K-feldspar, and hornblende, which are prevalent in the quartz diorite but almost completely absent in the saprolite, are not required to balance the pore water compositions. Only at shallower depths in the saprolite (1.52–1.83 m) are inconsistencies in the calculations evident (i.e., erroneous precipitation of quartz and biotite and extensive weathering of plagioclase). These errors are introduced because of significant temporal and spatial variations in pore water at shallower depths due to evapotranspiration and biologic cycling in the overlying soil zone.

Masses of reacted minerals generally increase with depth, as expected for sequentially longer flow paths and residence times (Fig. 9). Quartz contributes between 37% and 74% of the total dissolved silica in the pore waters in the saprolite based on the mineral stoichiometries (Table 3) and using the K-Fe-Si-Al constraints. Quartz contributions are lower (19–58%) using the Mg-Fe-Si-Al constraints. This difference reflects a lower Mg to K molar ratio in the biotite than in the pore waters, requiring more biotite and less quartz to react. Murphy et al. (1998) discuss the mechanisms and rates of biotite dissolution in the regolith in detail.

4.4. Rates of Quartz Weathering

The kinetic rate constant for quartz dissolution under field conditions in the Guaba Ridge saprolite k_{qtz} (mol m^{-2} s^{-1}) can be defined in terms of the expression

$$k_{qtz} = \frac{\Delta M_{qtz}}{S_s \Delta t} \tag{3}$$

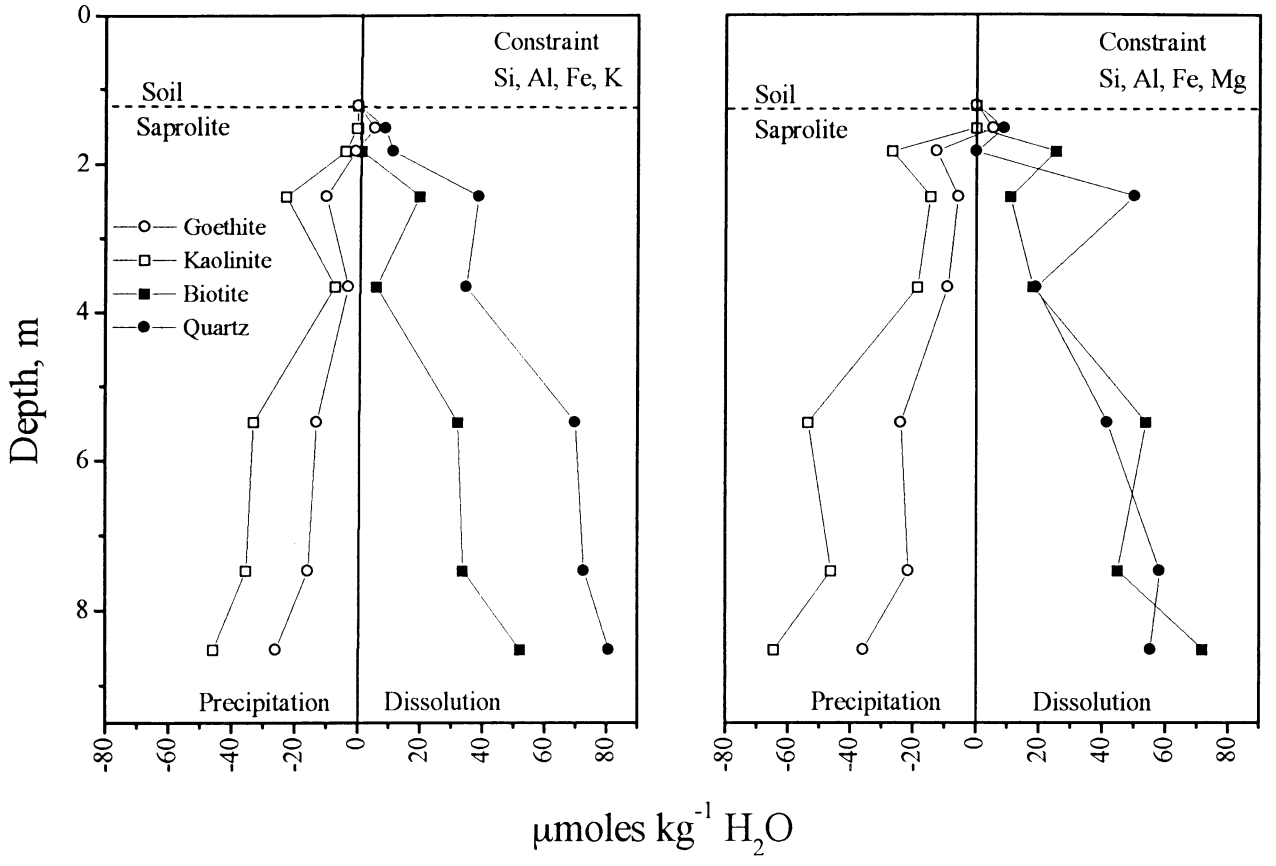

Fig. 9. Cumulative moles of minerals dissolved or precipitated required to balance observed changes in pore water concentrations. Results represent application of Si, Al, Fe, K, and Si, Al, Fe, Mg constraints as modeled by NETPATH to the mineral reactions.

where ΔM_{qtz} is the mass loss of quartz (mol), S_s is the total surface area of quartz grains (m^2) in the saprolite; and t is the time (s) over which weathering has occurred.

ΔM_{qtz} is the mass loss (Table 3) normalized to saprolite volume. The total quartz surface area S_s (m^2) exposed to pore water per volume is tabulated in Table 4 from the relationship

$$S_s = S_t q(1 - \eta)\rho z A \quad (4)$$

where S_t ($m^2\ g^{-1}$) is the specific quartz surface area, q is the average weight % of quartz in the saprolite (Table 4), η is the average porosity, (0.45), ρ is the density of quartz (2.65×10^6 g m^{-3}), z is the depth interval (m), and A is the area of saprolite surface (m^2). A specific quartz surface area S_t of 0.2 $m^2\ g^{-1}$ is used in Eqn. 4. This value corresponds to the average minimum surface areas of quartz grains in the upper saprolite (Fig. 8). These grains are least affected by contributions from Fe oxide fillings of microfractures observed in the overlying soil and by the persistence of partially weathered silicate inclusions in the deeper saprolite. The total surface area of quartz per volume of saprolite (S_s) is 1.9×10^4 to 4.5×10^5 m^2 (Table 4).

Table 4. Parameters describing rates of quartz dissolution.

Depth (m)	Travel Time del t (s)	Quartz % q	Surface Area S_t (m^2)	Qtz Rate (k_{qtz}) K-Fe-Si-Al	Qtz Rate (k_{qtz}) Mg-Fe-Si-Al
1.52	1.61E+07	21.7	1.90E+04	2.81E−15	2.85E−15
1.83	3.26E+07	21.87	3.89E+04	1.77E−15	
2.44	6.53E+07	22.87	8.13E+04	2.92E−15	3.78E−15
3.66	1.31E+08	19.94	1.42E+05	1.50E−15	8.18E−16
5.49	2.28E+08	22.06	2.75E+05	1.56E−15	9.26E−16
7.47	3.34E+08	20.61	3.76E+05	1.19E−15	9.48E−16
8.53	3.91E+08	21.34	4.55E+05	1.09E−15	7.45E−16

Table 5. A comparison of experimental rates of quartz dissolution with rate calculated for quartz weathering in the Guaba Ridge saprolite.

Log rate k_r (moles m^{-2} s^{-1})	Quartz type	Grain size (μm)	Surface area (m^{-2} g^{-1})	pH	Water/rock ratio (ml g^{-1})	Reference
−14.75	Igneous, Plutonic	450	0.2	~5	NA	Present study
−14.24	Ottawa Sand	590–850	0.023	7	0.8	Tester et al., 1994
	Montredon Labessonnie, France, Xtal	50	0.31	6.5	75	Berger et al., 1994
−12.9	Red Lake, Ontario, Xtal	30–75	0.17			Bennett, 1991
−12.44	Hot Springs, Arkanasas, XTal	74–149	0.11	5.5	31.1	Brady & Walther, 1990
−13.38	Corning Sand	125–100	0.92	5.5	30–100	Rimstidt & Barnes, 1980
−12.15	Synthetic	75–150	0.049	3	25–200	Casey et al., 1990

Calculation of the quartz dissolution rate requires the residence time of pore waters in contact with quartz grain surfaces (Δt, Eqn. 3). A hydraulic flux density of 6.14×10^{-9} m s^{-1} was estimated for the saprolite based on experimental unsaturated hydraulic conductivities and a field saturation of 73% (White et al., 1998). Travel times through portions of the profile are presented in Table 4. Pore water takes approximately 12 years (3.9×10^8 s) to travel the 7 m through the saprolite profile.

Calculated rates constants for quartz dissolution k_{qtz} (Eqn. 3) range between 9.48×10^{-16} to 1.09×10^{-15} mol m^{-2} s^{-1} depending on the specific depth interval and NETPATH constraint (Table 3) used to calculate quartz mass loss. Quartz weathering rates increase with decreasing depth, suggesting an increasing reaction rate in more dilute pore waters. The average dissolution rate for quartz weathering for the Guaba Ridge is $k_{qtz} = 10^{-14.8}$ mol m^{-2} s^{-1}.

The proportion of quartz loss during the weathering of the Guaba Ridge saprolite can be estimated from this average rate constant and the relationship

$$r = r^0 - (k_{qtz} V_0 \Delta t) \quad (5)$$

where r is the radius of the weathered grain (m), r^o is the radius of the original grain, V_o is the molar volume (2.26×10^{-5} m^3/mol or m^3 mol^{-1}), and Δt is the duration of weathering (Lasaga, 1984). In 100 Ka, a rate constant k_{qtz} of $10^{-14.8}$ mol m^{-2} s^{-1} reduces the average quartz grain from a radius of 0.23 mm (r^o) to 0.22 mm (r). This minor size reduction over a reasonable time estimate for saprolite formation is in agreement with the lack of discernible quartz loss (Fig. 2) or size reduction (Fig. 3). This supports the contention that significant amounts of quartz have not dissolved during the formation of the Guaba Ridge regolith.

The dissolution rate constant for natural weathering of Guaba Ridge quartz falls just below the range of experimental quartz dissolution constants at comparable pH and solute compositions reported in Table 5 ($10^{-12.1}$–$10^{-14.2}$ mol m^2 s^{-1}). This agreement contrasts with studies of other primary silicate minerals that have shown natural weathering rates to be 2 to 3 orders of magnitude slower than experimental rates (White and Brantley, 1995, and references therein). This similarity may reflect greater homogeneity in both the weathering environment and the mineral substrate. Quartz is both structurally and chemically simpler than other silicate minerals and also contains fewer impurities and defects. Preferential reaction at such sites can produce anomalously fast dissolution under short-term experimental conditions.

Differences in experimental and natural weathering rates have also been attributed to differing hydrologic conditions. Macropore flow and wetting and drying are commonly invoked processes, which decrease wettable surface areas, and thus reaction rates under natural conditions (Swoboda-Colberg and Drever, 1993; Velbel, 1993). However, the Guaba Ridge saprolite is texturally homogeneous and remains close to hydraulic saturation throughout the year, thus making the measured BET surface areas better estimates of surfaces exposed to pore water. Also such wet conditions maintain relatively low solute concentrations, which promote thermodynamically unsaturated conditions. The degree to which the quartz weathering rates measured in this tropical setting can be extrapolated to other weathering environments depends on the complex interaction of these factors.

5. CONCLUSIONS

This study presents one of the first detailed investigations that quantitatively describes quartz weathering in a natural environment. Determination of dissolution rates are made possible by extremely rapid weathering, a relatively simple regolith mineralogy, and detailed information on hydrologic and chemical transport in the tropical regolith environment. Even under these weathering conditions, the total mass loss of quartz is minor compared to other primary minerals. Morphologic evidence for weathering is apparent in solution rounding of angular features and the limited development of etch pitting on grain surfaces. Filling of fractures with secondary goethite and kaolinite explains the observed high surface area of quartz in the regolith soils. The persistence of highly weathered feldspar inclusions in quartz grains explains the trend of increasing surface area with depth in the saprolite.

Solute Si increases with fluid residence times in the saprolite. One difficulty in estimating quartz dissolution based on dissolved silica is separating the relative contributions made of dissolution of other silicate minerals, principally biotite and silica uptake by secondary kaolinite. The NETPATH computer code was utilized in this exercise to calculate contributions of quartz dissolution to silica pore water concentrations. Combining this contribution with specific quartz surface areas and the fluid residence time permitted calculation of weathering rate constants of 9.48×10^{-16} to 1.09×10^{-15} mol m^{-2} s^{-1} These rates just below the range reported for the experimental dissolution of quartz.

Acknowledgements—The authors would like to thank our colleagues: Robert Oscarson, U.S.G.S. Menlo Park, who assisted in the SEM

studies, and Tina Takagi who performed most of the grain size analyses. The authors also express thanks to Drs. Alex Blum, Susan Brantley and Ben Turner for helpful discussions and review of the manuscript. The manuscript was strengthened by reviews from Dr Patricia Dove, Dr Katherine Nagy and one anonymous reviewer. This work was greatly facilitated by Matt Larson and others of the Puerto Rico District Office of the U.S.G.S. who collected samples. This study was funded under the U.S.G.S. Global Change Program and the U.S. Geological Survey Water, Energy, and Biogeochemical Budgets (WEBB) Program.

REFERENCES

Alexandre A., Meunier J.-D., Colin F., and Koud J.-M. (1997) Plant impact on the biogeochemical cycle of silicon and related weathering processes. *Geochemica Cosmochemica Acta* **61,** 677–682.

Asumadu K., Gilkes R. J., Armitage T. M., and Churchward H. M. (1988) The effects of chemical weathering on the morphology and strength of quartz grains—an example from S.W. Australia. *Journal of Soil Science* **39,** 375–383.

Asumadu K., Gilkes R. J., Churchward H. M., and Armitage T. M. (1987) Detailed characterization of quartz grains in two sandy soils, western Australia. *Geoderma* **4,** 29–47.

Bennett P. C. (1991) Quartz dissolution in organic-rich aqueous systems. *Geochemica Cosmochemica Acta* **55,** 1781–1797.

Berger G., Cadore E., Schott J., and Dove P. M. (1994) Dissolution rate of quartz in lead and sodium electrolyte solutions between 25 and 300°C: Effect of the nature of surface complexes and reaction affinity. *Geochim. Cosmochim. Acta* **58,** 541–551.

Blatt H. (1967) Original characteristics of clastic quartz grains. *J. Sedimentary Petrology* **37,** 401–424.

Blum A. E., Yund R. A., and Lasaga A. C. (1990) The effect of dislocation density on the dissolution rate of quartz. *Geochim. Cosmochim. Acta* **54,** 283–297.

Boccheciamp R. A. (1977) Soil survey of the Humacao area of eastern Puerto Rico. *U.S. Department of Agriculture, Soil Conservation Service*, 103.

Brady P. V. and Walther J. V. (1990) Kinetics of quartz dissolution at low temperatures. *Chemical Geology* **82,** 253–264.

Brantley, S. L. , White, A. F. , and Hodson, M. E. (1999*) Surface Area of Primary Silicate Minerals* in "Growth and Dissolution in Geosystems" B. Jamtveit (ed.) Chapman and Hall.

Brantley S. L., Crane S. R., Crerar D., Hellmann R., and Stallard R. (1986) Dissolution at dislocation etch pits in quartz. *Geochim. Cosmochim. Acta* **50,** 2349–2361.

Brown E. T., Stallard R. F., Larsen M. C., Raisbeck G. M., and Yiou F. (1995) Denudation rates determined from the accumulation of in situ produced ^{10}Be in the Luquillo Experimental Forest, Puerto Rico. *Earth and Planetary Sciences Letters* **129,** 193–202.

Buffle J. (1988) *Complexation Reactions in Aquatic Systems: An Analytical Approach*. Wiley.

Cleary W. J. and Conolly J. R. (1972) Embayed quartz grains in soils and their significance. *Journal of Sedimentary Petrology* **42,** 899–904.

Crook K. A. W. (1968) Weathering and roundness of quartz sand grains. *Sedimentology* **11,** 171–182.

Darmody R. G. (1985) Weathering assessment of quartz grains: A semi-quantitative approach. *Soil Sci. Soc. Am. J.* **49,** 1322–1324.

Douglas L. A. and Platt D. W. (1977) Surface morphology of quartz and age of soils. *Soil Sci. Soc. Am. J.* **41,** 641–645.

Eswaran H. (1979) Surface textures of quartz in tropical soils. *Soil Sci. Soc. Am. J.* **43,** 420–424.

Fournier R. O. and Potter R. W. (1982) An equation correlating the solubility of quartz in water from 25°C to 900°C at pressures up to 10,000 bars. *Geochim. Cosmochim. Acta* **46,** 1969–1973.

Gratz A. J., Manne S., and Hansma P. K. (1991) Atomic force microscopy of atomic-scale ledges and etch pits formed during dissolution of quartz. *Science* **251,** 1343–1346.

Gratz A. J. and Bird P. (1993) Quartz dissolution: Theory of rough and smooth surfaces. *Geochim. Cosmochim. Acta* **57,** 977–989.

Heinisch H. L., Sines G., Goodman J. W., and Kirby S. H. (1975) Elastic stresses and self-energies of dislocations of arbitrary orientation in anisotropic media: Olivine, orthopyroxene, calcite, and quartz. *Journal of Geophysical Research* **80,** 1885–1896.

Herbillon A. J. (1980) Mineralogy of oxisols and oxic materials. In *Soils With Variable Charge* (ed. B. K. G. Theng), pp. 109–126. New Zealand Society of Soil Science.

Hicks B. D. (1985) Quartz dissolution features: An experimental and petrofabric study. M.S. Thesis, Univ. Missouri-Columbia.

Iler P. K. (1979) *The Chemistry of Silica*. Wiley & Sons.

Klute A. and Dirksen C. (1986) Hydraulic conductivity and diffusivity: Laboratory methods. In *Methods of Soil Analysis* (ed. A. Klute), pp. 687–699. Soil Sci Soc America.

Larsen M. C. and Torres-Sanchez A. J. (1989) Landslides triggered by Hurricane Hugo in eastern Puerto Rico, September, 1989. *Caribb. J. Sci.* **28,** 113–125.

Lasaga A. C. (1984) Chemical kinetics of water-rock interactions. *Journal of Geophysical Research* **89,** 4009–4025

Lasaga A. C. and Blum A. E. (1986) Surface chemistry, etch pits and mineral-water reactions. *Geochim. Cosmochim. Acta* **50,** 2363–2379.

Leamnson R. N., Thomas Jr. J., and Ehrlinger H. P. (1969) A study of the surface areas of particulate microcrystalline silica and silica sand. *Illinois State Geol. Surv. Cir.* **444,** 12p.

Lucas Y., Luizao F. J., Chauvel A., Rouiller J., and Nahon D. (1993) The relation between biological activity of the rain forest and mineral composition of soils. *Science* **260,** 521–523.

Malengreau N. and Sposito G. (1997) Short-time dissolution mechanisms of kaolinitic tropical soils. *Geochim. Cosmochim. Acta* **61,** 4297–4307.

Marcelino V. and Stoops G. (1996) A weathering score for sandy soil materials based on the intensity of etching of quartz grains. *European Journal of Soil Science* **47,** 7–12.

Mazzullo J. and Magenheimer S. (1987) The original shapes of quartz sand grains. *J. Sedimentary Petrology* **57,** 479–487.

Mehra O. P. and Jackson M. L. (1960) Iron oxide removal from soils and clays by a dithionite-citrate system buffered with sodium bicarbonate. In *Proceedings 7th National Conference on Clays and Clay Minerals* (ed. A. Swineford), pp. 317–327. Pergamon Press.

Morey G. W. and Hesselgesser J. M. (1951) The solubility of quartz and other substances in superheated steam at high pressures. *Amer. Soc. Mech. Eng. Trans.* **73,** 865–872.

Moss A. J. and Green P. (1975) Sand and silt grains: Predetermination of their formation and properties by microfractures in quartz. *Journal of the Geological Society of Australia* **22,** 485–495.

Murphy S. F., Brantley S. L., Blum A. E., White A. F., and Dong H. (1998) Chemical weathering in a tropical watershed, Luquillo Mountains, Puerto Rico II: Rate and mechanism of biotite weathering. *Geochim. Cosmochim. Acta* **62,** 227–243.

Nahon D. B. (1991) *Introduction to the Petrology of Soils and Chemical Weathering*. John Wiley & Sons, Inc.

Nesbitt H. W. and Young G. M. (1984) Prediction of some weathering trends of plutonic and volcanic rocks based on thermodynamic and kinetic considerations. *Geochim. Cosmochim. Acta* **48,** 1523–1534.

Nimmo J. R., Askin K. C., and Mello K. A. (1992) Improved apparatus for measuring conductivity at low water content. *Soil Science America Journal* **56,** 1788–1761.

Nooren C. A. M., van Breemen N., Stoorvogel J. J., and Jongmans A. G. (1995) The role of earthworms in the formation of sandy surface soils in a tropical forest in Ivory Coast. *Geoderma* **65,** 135–148.

Parks G. A. (1984) Surface and interfacial free energies of quartz. *Geophysical Research* **89,** 3997–4008.

Parks G. A. (1990) Surface energy and adsorption at mineral/water interfaces: An introduction. In *Mineral-Water Interface Geochemistry*, (ed. M. F. Hochella and A. W. White, A. F.), Vol. 23, pp. 133–169. Mineral. Soc. Amer. Reviews in Mineralogy.

Plummer L., Prestemon E. C., and Parkhurst D. L. (1991) An Interactive Code (NETPATH) for Modeling NET Geochemical Reactions Along A Flow Path. *Water Resources Investigation Reports 91-4078*, 227 p.

Pope G. A. (1995) Internal weathering in quartz grains. *Physical Geography* **16,** 315–338.

Pye K. and Sperling C. H. B. (1983) Experimental investigation of silt formation by static breakage processes: The effect of temperature,

moisture and salt on quartz dune sand and granitic regolith. *Sedimentology* **30,** 49–62.
Pye K. and. Mazzullo J. (1994) Effects of tropical weathering on quartz grain shape: An example from northeastern Australia. *Journal of Sedimentary Research* **A64**(3), 500–507.
Raeside J. D. (1959) Stability of index minerals in soils with particular reference to quartz, zircon, and garnet. *Journal of Sedimentary Petrology* **29**(4), 493–502.
Rimstidt, J. D. (1984) Quartz solubility at low temperatures. Geol. Soc. Amer. Abst. Annal. Mtg. 329.
Rimstidt J. D. (1997) Quartz solubility at low temperatures. *Geochim. Cosmochim. Acta* **61,** 2552–2558.
Rimstidt J. D. and Barnes H. L. (1980) The kinetics of silica-water reactions. *Geochim. Cosmochim. Acta* **44,** 1683–1699.
Robie R. A., Hemingway B. S., and Fisher J. S. (1979) Thermodynamic properties of minerals and related substances at 298.15 K and 1 bar (105 Pascals) pressure and at high temperatures. *U. S. Geol. Surv. Bull. 1452,* 465.
Seiders V. M. (1971) Cretaceous and lower Tertiary stratigraphy of the Gurabo and El Yunque Quadrangles, Puerto Rico. *Geological Survey Bulletin 1294-F,* 1–53.
Simon A., Larsen M. C., and Hupp C. R. (1990) The role of soil processes in determining mechanisms of slope failure and hillslope development in a humid-tropical forest, eastern Puerto Rico. *Geomorphology* **3,** 263–286.
Stonestrom D. A., White A. F., and Akstin K. C. (1998) Determining rates of chemical weathering in soils—Solute transport versus profile evolution. *J. Hydrol.* **209,** 331–345.
Sverdrup H. U. (1990) *The Kinetics of Base Cation Release Due to Chemical Weathering.* Lund University.
Swoboda-Colberg and Drever J. I. (1993) Mineral dissolution rates in plot-scale field and laboratory experiments. *Chemical Geology* **105,** 51–69.
Tester J. W., Worley W. G., Robinson B. A., Grigsby C. O., and Feerer J. L. (1994) Correlating quartz dissolution kinetics in pure water from 25 to 625°C. *Geochim. Cosmochim. Acta* **58,** 2407–2420.
Thomas M. F. (1994) *Geomorphology in the Tropics*. John Wiley & Sons.
Turner B. F., Brantley S. L., Stonestrom D. A., White A. F., and Larsen M. C. (1996) Solute transport and chemical weathering in a tropical rain forest saprolite, Puerto Rico. *Geol. Soc Amer., Abst., Denver,* A131.
Velbel, M. A. (1993) Constancy of silicate-mineral weathering ratios between natural and experimental weathering; implications for hydrologic control of differences in absolute rates. *Chemical Geology*. **105,** 89–99.
White A. F. and Blum A. E. (1995) Effects of climate on chemical weathering rates in watersheds. *Geochim. Cosmochim. Acta* **59,** 1729–1747.
White A. F., Blum A. E., Schulz M. S., Bullen T. D., Harden J. W., and Peterson M. L. (1996) Chemical weathering of a soil chronosequence on granitic alluvium 1. Reaction rates based on changes in soil mineralogy. *Geochim. Cosmochim. Acta* **60,** 2533–2550.
White A. F., Blum A. E., Schulz M. S., Vivit D. V., Larsen M., and Murphy S. F. (1998) Chemical weathering in a tropical watershed, Luquillo Mountains, Puerto Rico: Weathering rates based on mineral and solute mass balances. *Geochimica et Cosmochimica Acta* **62,** 209–226.
White A. F. and Brantley S. L. (1995) Chemical weathering rates of silicate minerals. In *Reviews in Mineralogy,* Vol. 31, pp. 584. Mineralogical Society of America.
White A. F. and Peterson M. L. (1990) Role of reactive surface area characterization in geochemical models. In *Chemical modeling of aqueous systems II* (eds. D. C. Melchior and R. L. Bassett), Vol. 416, pp. 461–475. ACS Symp. Series.
Williame C, Christie J. M., and Kovacs M. P. (1979) Electron microscope study of plastic deformation in experimentally deformed alkali feldspars. *Bullt. Soc. Fr. Mineral. Cryst.* **100,** 263–271.